Electron scattering from ^{9}Be

J. P. Glickman, W. Bertozzi, T. N. Buti,* S. Dixit,† F. W. Hersman,‡ C. E. Hyde-Wright§
M. V. Hynes,** R. W. Lourie,†† and B. E. Norum††
Department of Physics and Laboratory for Nuclear Science, Massachusetts Institute of Technology, Cambridge, Massachusetts 02139

J. J. Kelly
Department of Physics and Astronomy, University of Maryland, College Park, Maryland 20742

B. L. Berman
Department of Physics, George Washington University, Washington, D.C. 20052

D. J. Millener
Brookhaven National Laboratory, Upton, New York 11973
(Received 1 October 1990)

The structure of ^{9}Be is investigated using electron scattering measurements at 90° and 160° for momentum transfers between about 1.0 and 2.5 fm^{-1}. In addition to the $\frac{3}{2}^-$ ground state and the narrow $\frac{5}{2}^-$ state at 2.43 MeV, detailed line-shape analysis was used to extract cross sections for broad states at 1.68, 3.05, 4.70, 6.38, 6.76, 11.28, and 13.79 MeV. The previously unknown state at 6.38 MeV was isolated from the known 6.76 MeV state in both (e,e') and (p,p') data using the dependence of peak position upon momentum transfer. On the basis of the form factor, the 6.38 MeV state replaces the 6.76 MeV state as the $\frac{7}{2}^-$ member of the ground-state rotational band and the 6.76 MeV state is identified with the lowest $\frac{9}{2}^+$ state predicted by the shell model. The data for all states are compared with a shell-model calculation that uses the full $0\hbar\omega$ and $1\hbar\omega$ model spaces. Calculations are also presented for the narrow states between 14 and 18 MeV excitation.

I. INTRODUCTION

For p-shell nuclei it is possible to test extensive shell-model calculations with a large variety of reactions. In this paper, we compare $0\hbar\omega$ and $1\hbar\omega$ shell-model calculations for ^{9}Be with electron scattering data for all narrow states and several broad states below 18 MeV of excitation. In a companion paper, we report similar data for the scattering of 180 MeV protons.[1] We find that much insight into the structure of this nucleus can be obtained by comparing these reactions.

The only narrow states that are observed in ^{9}Be below 14 MeV excitation are the $\frac{3}{2}^-$ ground state and the 2.43 MeV state identified as the $\frac{5}{2}^-$ member of the ground-state rotational band. The $\frac{7}{2}^-$ member of that band is usually identified with the broad state listed at 6.76 MeV in standard compilations.[2] However, when (p,p') spectra are analyzed with a single Lorentzian peak in this region, the apparent position systematically shifts from about 6.4 to about 6.8 MeV as the momentum transfer increases.[3,4] The same systematic shift is observed in the present (e,e') data.

This result can be interpreted as evidence for the existence of two broad states of different multipolarities, with the state of lower multipolarity occurring lower in energy.[1] Electroexcitation of the rotational band should be dominated by a common $C2$ form factor. The lowest $\frac{9}{2}^+$ shell-model state should be excited predominantly via a $C3$ multipole and hence its form factor is expected to peak at larger momentum transfer than those of the rotational band. Therefore, we tentatively identify the new state observed at 6.38 MeV in this (e,e') experiment and in the (p,p') experiment of Dixit *et al.*[1] as the $\frac{7}{2}^-$ rotational state and identify the 6.76 MeV state as the previously unknown $\frac{9}{2}^+$ state. Hence, we believe that the Ajzenberg-Selove[2] assignment of $\frac{7}{2}^-$ to a single broad peak at 6.76 MeV is incorrect.

We have also obtained data for many other relatively broad states in ^{9}Be. Empirical fits to the form factor data were made using shell-model calculations whenever possible to determine the dominant multipoles. The shell-model calculations were performed using the Cohen and Kurath[5] interaction for p-shell matrix elements and the Millener and Kurath[6] interaction for cross-shell matrix elements. A more complete description of the calculation and the notation for the wave functions may be found in Ref. 7, which describes similar results for ^{13}C. Calculated and experimental energy levels are compared in Tables I and II. As detailed in Sec. IV, we tentatively identify the state at 11.28 MeV as $J^\pi=\frac{7}{2}^+$, $T=\frac{1}{2}$ and the state at 13.79 MeV as $J^\pi=(\frac{3}{2}^- - \frac{7}{2}^-)$, $T=\frac{1}{2}$.

We also compare calculations for four narrow states above 14 MeV with the electron scattering data of Lourie *et al.*[8] These states include the lowest $\frac{1}{2}^-$ and $\frac{3}{2}^-$ states with $T=\frac{3}{2}$ and two positive-parity states with $T=\frac{1}{2}$ that, according to Woods and Barker,[9] owe their narrow widths to parentage by a $2^+T=1$ excitation of the ^{8}Be

core. The present shell model calculation using a larger basis supports these assignments and is in good agreement with the form factor data.

The experiment and data analysis is described in Sec. II. The method used to analyze the form factors is presented in Sec. III. Our results are presented in Sec. IV and our conclusions are summarized in Sec. V.

II. EXPERIMENT AND DATA ANALYSIS

A. Experimental arrangement and analysis procedures

The experiment was performed at the MIT-Bates Linear Accelerator using the ELSSY spectrometer. Detailed descriptions of the spectrometer and detector systems may be found in Refs. 10 and 11. Data spanning momentum transfers between about 1.0 and 2.5 fm^{-1} were taken at angles of 90° and 160° using electrons with energies between 100 and 360 MeV. The beam energies were determined with precision better than 0.7 MeV from the differential recoil between beryllium and oxygen peaks observed using mixed-isotope BeO target foils. Data at 90° were collected using a pure ^{9}Be foil with thickness 26.76 mg/cm^2. Most of the data at 160° were taken with ^{9}Be targets with thicknesses of 18.65 and 23.16 mg/cm^2. A few spectra at 160° were taken with BeO targets ranging in thickness between 22.18 and 38.23 mg/cm^2. Cross sections were normalized according to the procedure of Lourie *et al.*[8] First, the ^{9}Be elastic cross section was obtained from measurements made with a BeO target normalized by comparing the ^{16}O cross section with phase-shift calculations using the known ^{16}O charge density.[12] Then, measurements with Be targets were normalized to this elastic cross section. This normalization procedure is most important at 160° where uncertainties of 1° in target angle are amplified by reflection geometry into 10% uncertainties in cross section. The required normalization factors were generally within 10% of unity.

The spectra were analyzed using the ALLFIT program[13] and methods described in Refs. 14 and 15. Narrow peaks were fitted using an empirical resolution function convoluted with a theoretical radiative response function. Broad peaks were described by Lorentzian line shapes [Ref. 14, Eq. (12)], using the positions and widths listed in Tables I and II and a threshold of 1.665 MeV, and were convoluted with the radiative response and the resolution function determined by the narrow peaks.

Given the limited momentum acceptance, two or three

TABLE I. *p*-shell wave functions for ^{9}Be using Cohen-Kurath (6–16) interaction.

J_n^π			$3/2_1^-$	$5/2_1^-$	$1/2_1^-$	$3/2_2^-$	$7/2_1^-$	$5/2_3^-$	$3/2_1^-$	$1/2_1^-$
T			1/2	1/2	1/2	1/2	1/2	1/2	3/2	3/2
E_{th} (MeV)[a]			0.	[2.43]	2.80	4.88	5.98	11.39	13.27	16.60
E_{exp} (MeV)[b]			0.	2.429(1)	2.78(12)		6.38(6)[c]	13.79(3)[d]	14.392(2)	16.975(1)
Γ (MeV)[b]					1.08(11)		1.2(2)[c]	0.59(6)		
$(\lambda\mu)$	L	S	SU3 amplitudes							
(31)	1	$\frac{1}{2}$	0.925		0.987	0.322				
(31)	2	$\frac{1}{2}$	−0.317	0.939		0.922		0.121		
(31)	3	$\frac{1}{2}$	−0.260				0.882	0.227		
	3	$\frac{3}{2}$					−0.263			
(12)	1	$\frac{1}{2}$	0.035		0.083	−0.107			0.922	0.959
	1	$\frac{3}{2}$	−0.089	0.112	−0.108	−0.006		−0.853		
	2	$\frac{1}{2}$	0.149	0.106		−0.088		0.165	−0.126	
	2	$\frac{3}{2}$	0.042	0.094	0.028	0.041	0.289	0.361		
	3	$\frac{1}{2}$	−0.017	0.078		0.045	0.209	0.015		
	3	$\frac{3}{2}$		0.007			−0.035	−0.008		
(20)	0	J	0.082		0.003	0.131			−0.233	0.139
	2	$\frac{1}{2}$	0.015	−0.051		0.019		0.123	0.209	
	2	$\frac{3}{2}$	0.021	−0.077	0.073	−0.074	0.150	0.027	0.097	0.239
(01)	1	$\frac{1}{2}$	−0.032		0.013	0.020			−0.061	0.054
	1	$\frac{3}{2}$	0.036	0.063	0.027	0.029		−0.066	−0.152	−0.032
	1	$\frac{5}{2}$	−0.003	0.007		0.013	0.042	0.169		

[a]Excitation energies were adjusted to place $5/2_1^-$ state at 2.43 MeV.

[b]Positions and widths from Ajzenberg-Selove (Ref. 2) unless noted otherwise.

[c]Position and width from Dixit *et al.* (Ref. 1).

[d]Electron scattering data for the state at 13.79 MeV are also consistent with theoretical form factors for $3/2_3^-$ (9.72 MeV), $7/2_2^-$ (10.03 MeV), or $5/2_4^-$ (12.87 MeV).

TABLE II. Wave functions for positive-parity states of ^{9}Be(e,e') with $T=\frac{1}{2}$.

J_n^π	E_{th} (MeV)[a]	E_{exp} (MeV)[b]	Γ (MeV)[b]	Weak-coupling amplitudes[d] $0^+\otimes sd$	$2^+\otimes d_{5/2}$	$2^+\otimes s_{1/2}$	$2^+\otimes d_{3/2}$
$1/2_1^+$	[1.68]	1.680(15)	0.200(20)	0.833	0.477		−0.197
$5/2_1^+$	2.87	3.049(9)	0.282(11)	0.708	−0.410	0.525	0.150
$3/2_1^+$	4.92	4.704(25)	0.743(55)	0.516	−0.399	0.676	−0.218
$9/2_1^+$	6.39	6.76(6)[c]	1.33(9)[c]		0.944		
$5/2_2^+$	7.52			0.471	−0.073	−0.740	0.071
$3/2_2^+$	8.17			0.587	−0.235	−0.587	−0.115
$7/2_1^+$	8.46	11.28(5)[c]	1.1(2)[c]		0.550		0.744
$1/2_2^+$	8.81			−0.390	0.751		−0.085
$3/2_3^+$	9.26			−0.258	−0.693	−0.069	0.494
$1/2_3^+$	11.08			0.050	0.199		0.838
$7/2_2^+$	12.01				0.647		−0.554

[a]Theoretical energies adjusted to place $1/2_1^+$ state at 1.68 MeV.
[b]Positions and widths from Ajzenberg-Selove (Ref. 2).
[c]Positions and widths from Dixit *et al.* (Ref. 1).
[d]Largest components of the form ^{8}Be$(J^+)\otimes sd(j)$.

spectrometer settings (bites) were required to cover 14 MeV of excitation. Because these data were acquired during experiments principally designed to study oxygen isotopes, these bites often had less than ideal coverage of the broad peaks in the beryllium spectrum. For example, the broad bump near 6.5 MeV was sometimes only partially covered by one of the bites. In such cases, we used the spectrum with the most complete coverage to determine the cross sections for the broad states and then entered fixed cross sections for these peaks into the analysis of other spectra in which these peaks were cut off. In this way the continuum could be made consistent between the bites.

The continuum was described by polynomial functions whose parameters were adjusted to ensure continuity across bites. The continuum rises fairly rapidly between about 1.6 and 6 MeV and then decreases gently for excitation energies between about 6 and 14 MeV. Therefore, we usually need either quadratic or cubic background functions to describe the continuum in this region of the spectrum. However, spectra which do not cover a large range of excitation energy can also be fitted equally well with linear backgrounds. The only peaks which are strongly affected by this ambiguity are the low-lying positive-parity states at 90°, which appear to have larger areas when linear instead of quadratic backgrounds are used. Also note that omission of the broad $\frac{1}{2}^-$ state at 2.78 MeV, which was seen in (p,p'),[1] has a similar effect upon these peaks. Use of quadratic backgrounds whose parameters are guided by spectra for higher excitation energies tends to alleviate both of these difficulties and improves the consistency of the 90° data for these peaks.

Typical spectra are shown in Figs. 1–3. There are only two narrow peaks below 14 MeV, namely, the $\frac{3}{2}^-$ ground-state and the $\frac{5}{2}^-$ state at 2.429 MeV. A continuum begins at 1.665 MeV, the threshold for ^{9}Be$\rightarrow{}^8$Be$+n$ break up. As illustrated by the 160° spectrum shown in Fig. 1, the peak corresponding to the $\frac{1}{2}^+$ state is rather asymmetric because it has a substantial intrinsic width, yet lies only 15 keV above threshold. The $\frac{5}{2}^+$ state at 3.05 MeV also appears most clearly at 160°.

Between 3 and 12 MeV there are several peaks with widths between about 0.3 and 1.5 MeV. Among the most prominent of these is a strong broad peak near 6.7 MeV and illustrated by Fig. 2. According to Dixit *et al.*,[1] this bump is actually composed of two broad peaks with the positions and widths listed in Tables I and II. Our

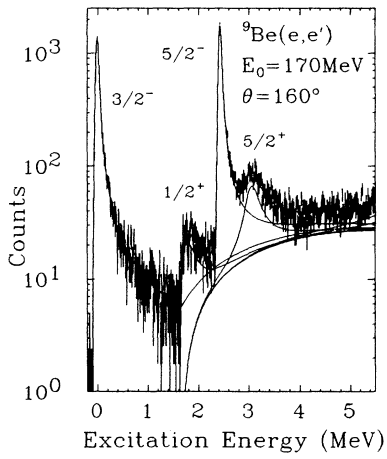

FIG. 1. Sample spectrum for the 0–5 MeV excitation region of ^{9}Be obtained by scattering 170 MeV electrons through 160°. Each peak, the continuum, and the total fit are shown. Notice that the $\frac{1}{2}^+$ peak lies just above the break-up threshold and is rather asymmetric.

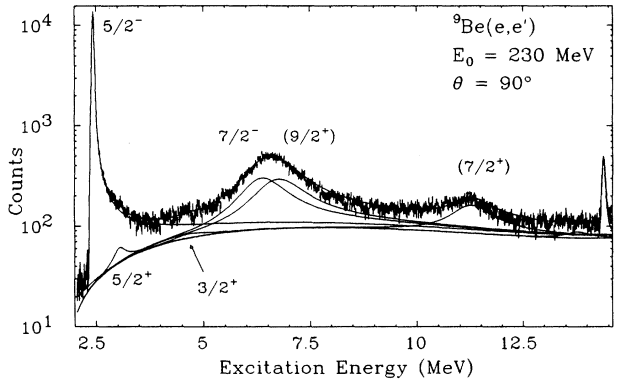

FIG. 2. Sample 90° spectrum for the 2–15 MeV excitation region obtained by scattering 230 MeV electrons through 90°. The broad peaks identified as $\frac{7}{2}^-$ and $\frac{9}{2}^+$ make similar contributions to the prominent 6.5 MeV bump. New assignments are indicated by parentheses.

analysis of this bump is described in the next section. Finally, there are several broad peaks observed between 11 and 14 MeV, illustrated in Fig. 3, whose line shape parameters are not well known. The analysis of these peaks is discussed in Sec. II C.

The cross sections we report represent the results of a final analysis in which the line shape parameters for the broad peaks were held constant. Therefore, the quoted uncertainties do not include contributions due to uncertainties in width. It is our experience that fitted cross sections are very nearly proportional to the assumed width of the peak because the fitted height of the peak is nearly independent of its width when the data do not strongly determine the width. Therefore, the shapes of the form factors are known better than their strengths. For the 6.5 MeV doublet, the sum of the two cross sections is determined more accurately than the individual contributions.

B. Interpretation of the 6.5 MeV bump

We have confirmed the presence of more than one resonance in the 6.5 MeV region by examining the dependence of the apparent position upon momentum transfer. Fits of the 90° spectra were made using a single Lorentzian of variable position and width in the vicinity of 6.5 MeV. The fitted position, relative to the narrow 2.429 MeV peak, is plotted in Fig. 4 as a function of momentum transfer. Some of the irregular fluctuations in position can be attributed to ambiguities in the background continuum and limitations in the momentum bite. Nevertheless, we find that the apparent position steadily increases from about 6.4 to 6.8 MeV over this range of momentum transfer, in agreement with the findings of Dixit *et al.*[1,3] We interpret this result as evidence for the presence of two broad peaks, with the state of lower multipolarity occurring lower in excitation energy. Unfortunately, the present data do not span a large enough range of momentum transfer to permit the line-shape parameters of the two peaks to be determined independently. Therefore, we use the line-shape parameters deduced by Dixit *et al.* to analyze the (e,e') spectra. A typical example is the 90° spectrum shown in Fig. 2, in which both the 6.38 and 6.76 MeV peaks make similar contributions to the strong bump centered near 6.5 MeV.

We also note that the references cited by the Ajzenberg-Selove compilation[2] also report positions that vary over the range between 6.4 and 6.8 MeV and that these positions can be correlated with momentum transfer in agreement with the present findings. For ex-

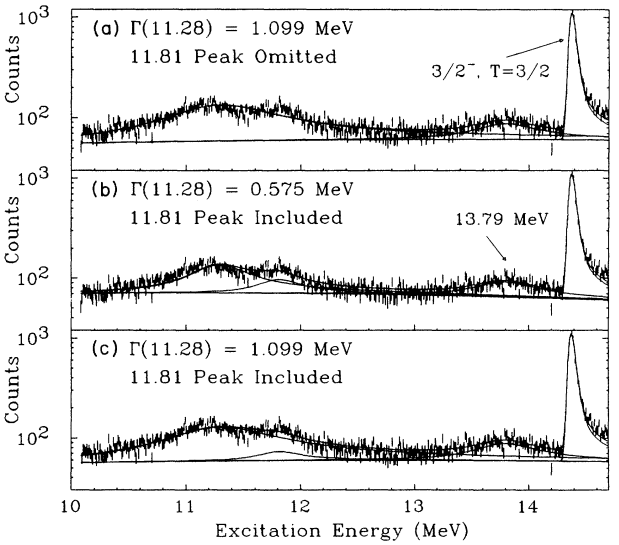

FIG. 3. Sample spectrum for the scattering of 180 MeV electrons through 160° with three analyses which show that the data favor the larger width for the 11.28 MeV peak and that the 11.81 MeV peak is present, but weak, at 160°. The 13.79 MeV peak is clearly evident in the 160° spectra.

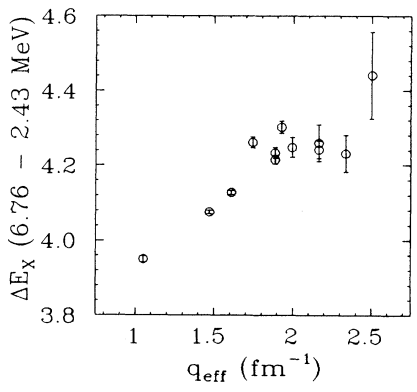

FIG. 4. The apparent separation between a Lorentzian peak near 6.5 MeV and the narrow peak at 2.429 MeV increases with momentum transfer, indicating the presence of an unresolved doublet containing two peaks of different multipolarities. These data are based upon fits made to 90° spectra.

ample, using electron scattering for momentum transfers below 1.5 fm^{-1}, Ngoc *et al.*,[16] Clerc *et al.*,[17] and Slight *et al.*[18] all report strong states with $C2$ angular distributions at 6.4 MeV. Ngoc *et al.*, in particular, analyzed their data for that state in terms of the rotational model. However, a variety of transfer and inelastic scattering reactions report positions ranging from 6.4 to 6.8 MeV with little agreement on width.[2] The discrepancies between these reactions may be attributed to their incomplete description of the spectrum.

C. Analysis of the 11.28 MeV peak

The analysis of proton scattering data made by Dixit *et al.*[1] produced a width $\Gamma(11.28)=1.10\pm0.23$ MeV for the state at 11.28 MeV that is almost twice as large as the width $\Gamma(11.28)=0.575\pm0.050$ MeV compiled by Ajzenberg-Selove.[2] The latter value is based upon two transfer reactions. Using the ^{7}Li(^{3}He,p) reaction, Cocke[19] deduced a width of 620±70 keV; however, the 11.28 MeV peak was partially obscured by a stronger peak at 11.81 MeV. A similar value was found by Ajzenberg-Selove *et al.*[20] using the ^{10}B(^{3}H,α) reaction, for which interference from the 11.81 MeV peak seems to be less important. Finally, Hasselgren *et al.*[21] reported a width in the range 0.5–1.0 MeV based upon a (p,p') experiment. However, the smaller values did not give a good description of Dixit's (p,p') spectra.[1]

We analyzed the (e,e') spectra twice, once with a width of 0.575 MeV and again with a width of 1.10 MeV for the 11.28 MeV state. Examples of these fits are shown in Fig. 3. When the smaller width is used, the fit tends to fall below the low-excitation side of the 11.28 MeV peak. However, only a very slight preference, on the basis of χ^2, was obtained for the larger width, so that the electron scattering data do not determine the width of this state unambiguously. The cross sections fitted to the 11.28 MeV state are effectively proportional to the assumed width because the fitted peak height is almost independent of width. Therefore, although the shape of the 11.28 MeV form factor is well determined by the data, an uncertainty in the overall scale that is perhaps as large as a factor of 2 must be considered when comparing to shell-model calculations.

Unfortunately, the results for the 11.81 MeV state are strongly affected by the ambiguity in the width of the 11.28 MeV peak. As also shown in Fig. 3, the analysis of the 160° data clearly indicates the presence of the 11.81 MeV peak with either width for the 11.28 MeV peak. However, use of the larger width reduces the cross sections fitted to the 11.81 MeV peak, especially at 90° where nonzero results for the 11.81 MeV state could only be obtained using a narrow width for the 11.28 MeV peak. Because of these ambiguities, we do not quote results for the 11.81 MeV state. Fortunately, no cross sections for states other than those at 11.28 and 11.81 MeV are affected by these ambiguities.

D. Analysis of other broad peaks

The state at 4.70 MeV is identified as $\frac{3}{2}^+$ but its large width and small strength make it very difficult to extract the $\frac{3}{2}^+$ peak from the much stronger 6.5 MeV peaks, the continuum, and the tail of the $\frac{5}{2}^-$ peak. The low-q data at 160° were usually collected with BeO targets and with momentum bites that were suitable for ^{16}O but unfavorable for the $\frac{3}{2}^+$ state of ^{9}Be. The larger-q data at 160° usually did not have enough statistics to permit reliable extraction of the $\frac{3}{2}^+$ peak. Although the peak was more prominent at 90°, where the data are less ambiguous, the absence of backward angle data for this state is probably an artifact of the experiment that does not reflect the relative strengths of the transverse and longitudinal form factors.

The peak at 13.79 MeV was clearly visible at 160°, as shown in Fig. 3, but was virtually absent at 90°. Hence, that state appears to be predominantly transverse. A peak at 7.94 MeV was also included in the analysis, but was too weak to obtain reliable extractions from stronger neighbors with uncertain widths. The broad $\frac{1}{2}^-$ state at 2.78 MeV was not clearly evident in any of the spectra and was omitted from the analysis.

E. From factor data

Form factors measured at 90° and 160° are compared in Fig. 5. The rather small differences between forward and backward angles that are observed for the $\frac{5}{2}^-$ and $\frac{7}{2}^-$ states indicate dominance of the longitudinal form factor. These two form factors appear to share similar $C2$ shapes. A small transverse form factor is evident for the $\frac{5}{2}^-$ state, but the transverse contribution to the $\frac{7}{2}^-$ data is too small to extract. Similarly, the ground-state data show significant magnetic contributions. Except for the $\frac{3}{2}^+$ state, all of the positive-parity states show large or even dominant transverse form factors. These data are examined in more detail in Sec. IV.

Experimental cross sections are compiled in Table III. Additional electron scattering data for some of these states is available from Refs. 16–18 and 22–26. We include these data in our subsequent analysis whenever adequate agreement is found for overlapping momentum transfers. Most discrepancies between previous results for some of the broad states and the present data can be attributed to deficiencies in the methods of analysis available to earlier experiments.

III. ANALYSIS OF FORM FACTORS

A. Electron scattering

Electron scattering calculations were performed using the plane-wave Born approximation, in which the cross section takes the form[27]

$$\frac{d\sigma}{d\Omega}=Z^2\sigma_M\eta\left[V_L(\theta)\sum_J|F_J^L|^2+V_T(\theta)\sum_J|F_J^T|^2\right], \quad (1)$$

where Z is the atomic number of the target nucleus and θ is the scattering angle. The point-charge cross section is given by

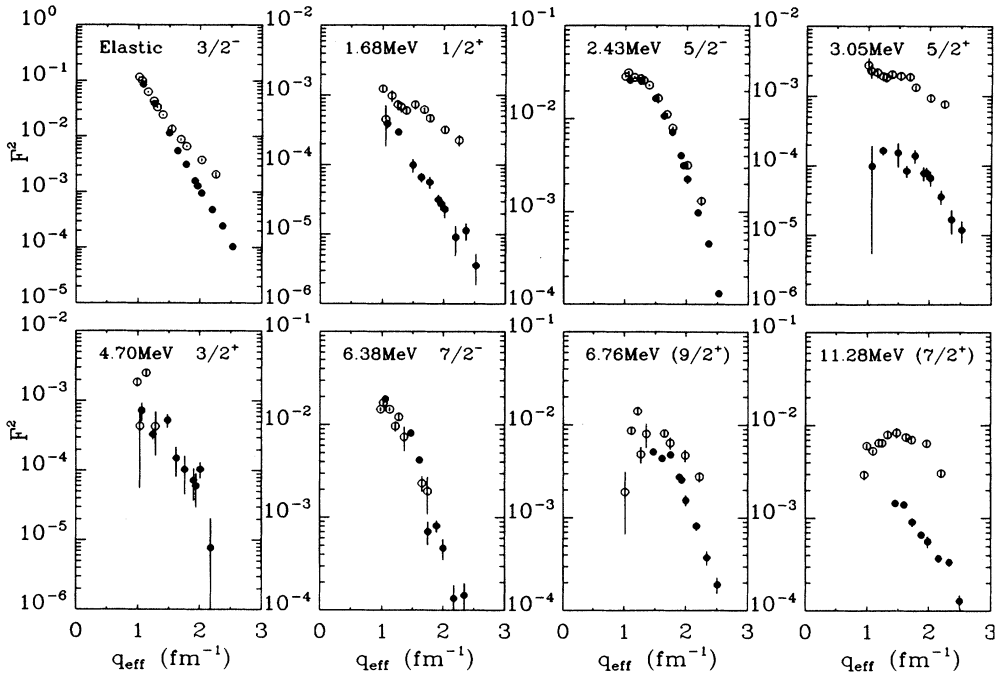

FIG. 5. Form factors measured at 90° are plotted as closed circles and data for 160° as open circles. Notice that the enhancement of the 160° data indicates substantial transverse form factors for the positive-parity states, but that the proposed $\frac{7}{2}^-$ state is almost purely longitudinal.

$$\sigma_M = \left[\frac{\alpha}{2E_0}\right]^2 \frac{\cos^2(\theta/2)}{\sin^4(\theta/2)} , \tag{2}$$

where E_0 is the incident energy and α is the fine-structure constant. The recoil factor is given by

$$\eta = \left[1+\frac{k_f - k_i\cos\theta}{E_T}\right]^{-1} , \tag{3}$$

where k_i (k_f) is the initial (final) momentum and E_T is the total energy (including rest mass) of the recoil nucleus. The angular factors

$$V_L(\theta) = q_\mu^4/q^4 , \tag{4a}$$

$$V_T(\theta) = \frac{|q_\mu^2|}{2q^2} + \tan^2\frac{\theta}{2} , \tag{4b}$$

where q^2 and q_μ^2 are the squares of the three- and four-momentum transfers, respectively, govern the relative weights of the longitudinal and transverse form factors. Distortion corrections are made by replacing the asymptotic momentum transfer with the effective local momentum transfer[28]

$$q \rightarrow q_{\text{eff}} = q\left[1-\frac{V_c(r_e)}{E_0}\right] , \tag{5}$$

where V_c is the Coulomb energy at the approximate electron radius $r_e = (L+1)/q$ and L is the minimum orbital angular momentum transfer for a particular transition.

The nuclear structure is described by longitudinal Coulomb (C), transverse electric (E) and transverse magnetic (M) form factors of the form[27]

$$F_J^C(q) = \frac{\sqrt{4\pi}}{Z}\frac{\hat{J}_f}{\hat{J}_i}\left\langle f\left|\left|\int d^3r\, \mathcal{Y}_J(q,\mathbf{r})\rho(\mathbf{r})\right|\right|i\right\rangle , \tag{6a}$$

$$F_J^E(q) = \frac{\sqrt{4\pi}}{Z}\frac{\hat{J}_f}{\hat{J}_i}\left\langle f\left|\left|\int d^3r \frac{1}{q}\nabla\otimes\mathcal{Y}_{JJ}(q,\mathbf{r})\cdot\mathbf{I}(\mathbf{r})\right|\right|i\right\rangle , \tag{6b}$$

$$F_J^M(q) = \frac{\sqrt{4\pi}}{Z}\frac{\hat{J}_f}{\hat{J}_i}\left\langle f\left|\left|\int d^3r\, \mathcal{Y}_{JJ}(q,\mathbf{r})\cdot\mathbf{I}(\mathbf{r})\right|\right|i\right\rangle , \tag{6c}$$

where $(\rho,\mathbf{I})$ is the nuclear 4-current operator and where $\hat{x} = \sqrt{2x+1}$. Scalar and vector solid harmonics are defined by

$$\mathcal{Y}_{JM}(q,\mathbf{r}) = \mathcal{J}_J(qr)Y_{JM}(\hat{r}) , \tag{7a}$$

$$\mathcal{Y}_{LJM}(q,\mathbf{r}) = \mathcal{J}_L(qr)[Y_L(\hat{r})\otimes\hat{\mathbf{e}}]_{JM} , \tag{7b}$$

where $\mathcal{J}_L(x)$ is a spherical Bessel function and $Y_{JM}(\hat{r})$ is an ordinary spherical harmonic.

B. Rosenbluth separation

It is useful to parametrize the form factors using the polynomial-Gaussian expansion (PGE)[14]

TABLE III. ^{9}Be(e,e') cross sections in *mb/sr* for scattering angles of 90° and 160°. Columns are labeled by excitation energy in MeV and multipolarity, with suggested assignments enclosed by parentheses. Uncertainties in the last one or two significant figures are given in parentheses and the power of 10 by the trailing exponent.

E_0 (MeV)	Elastic $\frac{3}{2}^-$	1.68 $\frac{1}{2}^+$	2.43 $\frac{5}{2}^-$	3.05 $\frac{5}{2}^+$	4.70 $\frac{3}{2}^+$	6.38 $\frac{7}{2}^-$	6.76 $(\frac{9}{2}^+)$	11.28 $(\frac{7}{2}^+)$	13.79 $(\frac{3}{2}^- - \frac{7}{2}^-)$
				Scattering angle $\theta=90.0°$					
149.4(5)	6.34(21)$^{-4}$	2.84(38)$^{-6}$	1.91(6)$^{-4}$	7.2(6.8)$^{-7}$	5.3(1.5)$^{-6}$	1.38(6)$^{-4}$			
175.1(4)	2.06(8)$^{-4}$	1.57(8)$^{-6}$	1.35(5)$^{-4}$	8.7(1.2)$^{-7}$	1.77(28)$^{-6}$				
209.2(2)	4.24(17)$^{-5}$	3.70(78)$^{-7}$	6.15(25)$^{-5}$	5.7(2.1)$^{-7}$	1.96(41)$^{-6}$	3.02(14)$^{-5}$	1.90(10)$^{-5}$	5.36(30)$^{-6}$	
229.0(2)	1.69(4)$^{-5}$	2.04(30)$^{-7}$	3.31(5)$^{-5}$	2.60(49)$^{-7}$	4.7(2.1)$^{-7}$	1.28(5)$^{-5}$	1.35(6)$^{-5}$	4.31(20)$^{-6}$	3.7(1.2)$^{-7}$
248.4(3)	8.13(27)$^{-6}$	1.48(27)$^{-7}$	1.88(6)$^{-5}$	3.64(79)$^{-7}$	2.7(1.5)$^{-7}$	1.84(52)$^{-6}$	1.26(7)$^{-5}$	2.37(23)$^{-6}$	
268.8(3)	3.55(9)$^{-6}$	7.0(1.3)$^{-8}$	8.98(21)$^{-6}$	1.75(40)$^{-7}$	1.61(79)$^{-7}$	1.80(26)$^{-6}$	6.16(23)$^{-6}$	1.48(11)$^{-6}$	1.06(57)$^{-7}$
274.8(7)	2.74(13)$^{-6}$	5.9(1.1)$^{-8}$	6.74(32)$^{-6}$	1.70(32)$^{-7}$	1.28(65)$^{-7}$		5.49(36)$^{-6}$		
284.3(3)	1.91(20)$^{-6}$	4.6(1.2)$^{-8}$	4.49(47)$^{-6}$	1.33(31)$^{-7}$	2.08(55)$^{-7}$	9.3(2.3)$^{-7}$	3.08(40)$^{-6}$	1.12(15)$^{-6}$	
309.0(6)	8.08(65)$^{-7}$	1.52(69)$^{-8}$	1.64(9)$^{-6}$	6.0(1.4)$^{-8}$	1.3(2.1)$^{-8}$	2.25(88)$^{-7}$	1.38(14)$^{-6}$	6.20(61)$^{-7}$	
333.6(3)	3.51(33)$^{-7}$	1.62(44)$^{-8}$	6.49(57)$^{-7}$	2.39(92)$^{-8}$		2.08(73)$^{-7}$	5.36(92)$^{-7}$	4.82(43)$^{-7}$	
357.5(7)	1.29(8)$^{-7}$	4.5(2.1)$^{-9}$	1.63(11)$^{-7}$	1.47(51)$^{-8}$			2.37(47)$^{-7}$	1.59(26)$^{-7}$	
				Scattering angle $\theta=159.79°$					
100.5(2)	3.08(6)$^{-5}$	3.26(36)$^{-7}$	7.55(12)$^{-6}$	7.4(1.9)$^{-7}$	4.89(63)$^{-7}$	3.86(19)$^{-6}$		7.75(88)$^{-7}$	
105.0(5)	2.43(10)$^{-5}$	1.08(64)$^{-7}$	7.61(32)$^{-6}$	5.6(1.2)$^{-7}$	1.05(92)$^{-7}$	4.15(30)$^{-6}$	4.6(3.0)$^{-7}$	1.46(8)$^{-6}$	2.62(71)$^{-7}$
115.3(3)	1.26(4)$^{-5}$	1.97(37)$^{-7}$	5.59(17)$^{-6}$	4.40(72)$^{-7}$	5.00(41)$^{-7}$	2.91(13)$^{-6}$	1.74(12)$^{-6}$	1.06(5)$^{-6}$	6.71(39)$^{-7}$
125.0(3)	7.32(26)$^{-6}$	1.24(21)$^{-7}$	4.63(17)$^{-6}$	3.28(47)$^{-7}$		1.63(20)$^{-6}$	2.38(19)$^{-6}$	1.10(10)$^{-6}$	4.56(53)$^{-7}$
130.4(1)	5.21(12)$^{-6}$	1.06(18)$^{-7}$	4.06(10)$^{-6}$	2.89(41)$^{-7}$	6.7(4.1)$^{-8}$	1.88(14)$^{-6}$	7.5(1.5)$^{-7}$	1.01(10)$^{-6}$	4.59(81)$^{-7}$
139.7(1)	3.30(9)$^{-6}$	8.14(93)$^{-8}$	3.12(8)$^{-6}$	2.79(25)$^{-7}$		1.0(3)$^{-6}$	1.09(31)$^{-6}$	1.08(7)$^{-6}$	4.89(49)$^{-7}$
154.6(5)	1.48(18)$^{-6}$	8.1(1.1)$^{-8}$	1.84(22)$^{-6}$	2.15(30)$^{-7}$				9.2(1.2)$^{-7}$	3.05(46)$^{-7}$
169.9(3)	7.99(39)$^{-7}$	5.61(40)$^{-8}$	1.02(3)$^{-6}$	1.72(16)$^{-7}$		2.12(39)$^{-7}$	7.36(54)$^{-7}$	6.78(66)$^{-7}$	1.50(16)$^{-7}$
179.5(2)	5.36(18)$^{-7}$	3.79(35)$^{-8}$	6.49(22)$^{-7}$	1.08(9)$^{-7}$		1.56(67)$^{-7}$	5.22(75)$^{-7}$	5.71(32)$^{-7}$	1.32(12)$^{-7}$
204.9(4)	2.35(13)$^{-7}$	1.98(23)$^{-8}$	1.97(11)$^{-7}$	5.79(58)$^{-8}$			2.93(43)$^{-7}$	3.98(35)$^{-7}$	6.0(1.2)$^{-8}$
228.9(7)	1.02(10)$^{-7}$	1.11(20)$^{-8}$	6.49(70)$^{-8}$	3.77(47)$^{-8}$			1.38(17)$^{-7}$	1.50(15)$^{-7}$	2.26(83)$^{-8}$

$$F_J^C(q)=\frac{\sqrt{4\pi}}{Z}\frac{q^J}{(2J+1)!!}f(q)e^{-y}\sum_\nu A_\nu y^\nu , \tag{8a}$$

$$F_J^E(q) =-\frac{\omega}{q}\left[\frac{J+1}{J}\right]^{1/2}\frac{\sqrt{4\pi}}{Z}\frac{q^J}{(2J+1)!!}f(q)e^{-y}\sum_\nu B_\nu y^\nu , \tag{8b}$$

$$F_J^M(q)=\left[\frac{J+1}{J}\right]^{1/2}\frac{\sqrt{4\pi}}{Z}\frac{q^J}{(2J+1)!!}f(q)e^{-y}\sum_\nu B_\nu y^\nu , \tag{8c}$$

where $y=(qb/2)^2$ and where b is an appropriate oscillator parameter. The connection between the polynomial coefficients A_ν and B_ν and the shell model is simplest when the auxiliary form factor $f(q)$ is taken as the product of single-nucleon and center-of-mass form factors $f_{\rm SN}$ and $f_{\rm c.m.}$ where[27]

$$f_{\rm SN}(q)=\left[1+\left[\frac{q}{\Lambda}\right]^2\right]^{-2} , \tag{9a}$$

$$f_{\rm c.m.}(q)=e^{y/A} \tag{9b}$$

and where $\Lambda=4.33$ fm^{-1}. This representation satisfies Siegert's theorem[29] provided that $B_0=A_0$ for transverse-electric multipoles. It is also useful to observe that irrotational flow within an incompressible liquid drop[30] requires $B_\nu=A_\nu$ for all ν. This condition can be applied when the transverse-electric form factor is too small to extract uniquely. Finally, the normalization factors in Eq. (8) are chosen so that $B(EJ)=A_0^2$ for normal-parity and $B(MJ)=B_0^2$ for abnormal-parity multipoles.

When the ground-state spin $J_i>0$, several multipoles can contribute to the excitation of each state. Under these conditions, it is usually not possible to extract from the data unique form factors for each multipole. Hence, for each state, we restrict the analysis to those multipoles which the shell model predicts will be dominant. Furthermore, we limit the number of terms in each polynomial according to the harmonic-oscillator model. Finally, when the transverse-electric form factor is small, we assume incompressible, irrotational flow.

It is usually more useful to display the data in terms of separated longitudinal and transverse form factors instead of at the two angles 90° and 160°. To make this separation, we fit the total data set using the functions described above. Longitudinal "data" are then produced by subtracting the fitted transverse form factor from the data acquired at forward angles. The estimated uncertainty in the fitted transverse form factor is included in the uncertainty quoted for the longitudinal data. Similarly, transverse "data" are extracted by subtracting the fitted longitudinal form factor from the backward-angle data and suitably increasing their uncertainties.

The principal advantage of this procedure is that it is not necessary to possess data at angle pairs with precisely matching momentum transfer. Furthermore, local fluctuations tend to be smoothed by subtracting a fitted quantity sensitive to a broad range of q. The principal disadvantage of this procedure is that if either the transverse or longitudinal form factor is especially small, deviations between the fit and the data for the strong form factor produce artificially large variations in the separated data for the weak form factor. For example, the square of the transverse form factor may appear negative if the fitted longitudinal form factor is above the data for backward angles. Nevertheless, for most of the states studied here, either one form factor is sufficiently dominant or the data are adequate to determine both form factors with relatively little ambiguity.

C. Form factors from the shell model

Shell model form factors were calculated using harmonic-oscillator wave functions with $b=1.765$ fm. Standard finite-size and center-of-mass corrections were applied according to Eq. (9). Except for the elastic $C0$ multipole, effective charges of $e_0=1+\delta e_p+\delta e_n=1.6e$ and $e_1=1+\delta e_p-\delta e_n=0.7e$ were used. These values are typical of $C2$ and $C3$ excitations in the p shell and the sd shell.[7,31] Magnetic multipoles were not renormalized, except as noted in the text. To ensure consistency with Siegert's theorem, transverse-electric multipoles were computed from the modified operator[32]

$$T_{JM}^E=\left[-\frac{\omega}{q}+\frac{q}{2m}\right]\left[\frac{J+1}{J}\right]^{1/2}\int d^3r\,\psi_f^* e\,\mathcal{Y}_{JM}(q,\mathbf{r})\psi_i - \frac{q}{m}\left[\frac{2J+1}{J}\right]^{1/2}\int d^3r\,\psi_f^* e\,\mathcal{Y}_{J+1,JM}\cdot\frac{1}{q}\nabla\psi_i + \frac{q}{2m}\int d^3r\,\psi_f^*\mathcal{Y}_{JJM}\cdot\boldsymbol{\mu}\psi_i \tag{10}$$

evaluated as a sum over single-particle orbitals with effective charge e and magnetic moment operator $\boldsymbol{\mu}=\mu\boldsymbol{\sigma}$.

IV. RESULTS

In this section, we compare theoretical predictions for the form factors with the data and empirical fits based upon the PGE. Wherever possible, the shell model is used to guide the choice of dominant multipoles and to constrain the fits. The fitted parameters are collected in Table IV and the electromagnetic moments are compared with shell-model predictions in Table V.

A. Ground state rotational band

The simplest model for ^{9}Be consists of two α particles covalently bound by a valence neutron. The ground state of such a system would be highly deformed and would exhibit a rotational band based upon the $\frac{3}{2}^-$ ground state. The clearest example of this structure is provided by the $\frac{5}{2}^-$ state, whose longitudinal form factor is expected to be almost pure $C2$. Using two terms of the PGE for the $C2$ form factor and assuming irrotational flow, we performed a Rosenbluth fit to the data for the $\frac{5}{2}^-$ state. The fitted

TABLE IV. PGE fits to ^{9}Be(e,e') form factors.

E (MeV)	State	ΔJ^π	A_0[a]	A_1	A_2	B_0	B_1
0	$\frac{3}{2}^-$	0^+	[1.1284][b]	−0.306(6)	−0.0395(3)		
		1^+				0.0769(2)	−0.0756(4)
		2^+[c]	4.13(6)	−0.355(5)			
		3^+				2.09(7)	
2.43	$\frac{5}{2}^-$	1^+				0.95(1)	−0.075(4)
		2^+	6.79(4)	−0.58(2)		[6.79]	[−0.58]
		3^+				0.73(21)	
6.38	$\frac{7}{2}^-$	2^+	5.80(9)	−1.33(5)			
		2^+[c]	4.05(4)	−0.33(1)			
1.68	$\frac{1}{2}^+$	1^-	0.185(8)	−0.028(6)		[0.185]	−3.42(16)
		2^-				0.15(3)	−0.13(1)
4.70	$\frac{3}{2}^+$	1^-	0.18(1)			[0.18]	
3.05	$\frac{5}{2}^+$	1^-	0.17(2)	−0.09(2)		[0.17]	[−0.09]
		2^-				0.40(3)	−0.18(2)
		3^-	0.95(29)			[0.95]	
		4^-				7.6(2)	
11.28	$(\frac{7}{2}^+)$[d]	3^-	7.5(4)	−0.4(2)		[7.5]	38.6(7)
6.76	$(\frac{9}{2}^+)$[d]	3^-	14.7(2)			[14.7]	
		4^-				13.2(6)	

[a]Coefficients A_ν and B_ν are in units of fm$^{\Delta J}$.
[b]Square brackets indicate fixed parameter for A_ν or for B_ν that the parameter is constrained to A_ν.
[c]Obtained by scaling $C2$ fitted to $5/2_1^-$.
[d]Suggested multipolarity.

form factors are shown in Fig. 6. The shape of the $C2$ form factor was then used for the $C2$ contributions to the $\frac{3}{2}^-$ and $\frac{7}{2}^-$ states, with only the strengths allowed to vary. Three terms of the $C0$ form factor were adjusted for the $\frac{3}{2}^-$ state. In the absence of a clear need for $C4$ excitation, this multipole was omitted for both $\frac{5}{2}^-$ and $\frac{7}{2}^-$ states.

The $C2$ form factor fitted to the $\frac{5}{2}^-$ state provides a good fit to both the $\frac{7}{2}^-$ data and the elastic data for $q \geq 1.5$ fm^{-1}. From the strength of the elastic $C2$ form factor, we deduce a quadrupole moment $Q = 5.9 \pm 0.1$ e fm^2 in good agreement with the value 5.3 ± 0.3 from hyperfine measurements.[34] We also note from Table IV that the relative strengths of the $\frac{5}{2}^-$ and $\frac{3}{2}^-$ states are in good accord with the rotational model, which predicts that the $B(C2)$ values for the $\frac{3}{2}^-$, $\frac{5}{2}^-$, and $\frac{7}{2}^-$ states should follow the ratios $1:\frac{18}{7}:\frac{10}{7}$. However, with the scale-factor analysis the $\frac{7}{2}^-$ form factor is only about half the intensity predicted by that model.

Shell-model calculations for the ground-state rotational band are compared with the data in Fig. 7. The longitudinal form factor is described very well for the $\frac{3}{2}^-$ state. Using standard effective charges $e_0 = 1.6$ e and $e_1 = 0.7$ e for the $C2$ form factors gives good agreement with the form factor for the $\frac{5}{2}^-$ state and with the $C2$ contribution to elastic scattering, although the quadrupole moment is smaller than either the hyperfine measurement or the (e,e') analysis. Nevertheless, good agreement with the elastic form factor at high-q is obtained through enhancement of the second maximum of the $C0$ form factor. The shape of the $C2$ form factor, on the other hand, appears to peak at a momentum transfer that is slightly too large. We also observe that the shell-model calculation for the $\frac{7}{2}^-$ state is almost identical with the scale-factor fit and also peaks too far out. Finally, the shell model predicts strengths in the ratio 1:3.41:1.35 compared with the rotational model 1:2.57:1.43. Thus, the shell model enhances the strength of the $\frac{5}{2}^-$ state relative to the ground state.

Alternatively, the fit to the data for the $\frac{7}{2}^-$ state can be improved considerably by allowing the shape of the $C2$ form factor to vary. With a more flexible shape, the fitted form factor is larger at its peak, but falls more rapidly with momentum transfer. Allowing for this shape difference, the ratio of strengths 1:2.69:1.92 agrees well with the rotational model. If this difference in form factor is taken seriously, it would indicate a stretching of the quadrupole density for higher spins. However, in the absence of reliable data at low momentum transfer, it is difficult to determine the shape of the form factor or to uniquely determine its peak. Although a broad bump with $C2$ characteristics has been observed in several previous low-q experiments,[16–18] the analysis techniques were not conducive to reliable extractions.

TABLE V. Electromagnetic matrix elements for ^{9}Be(e,e').

E_{exp} (MeV)	E_{th} (MeV)	J_n^π	Matrix element[a]	(e,e')[b]	Other	Theory[c]
0	0	$3/2_1^-$	$Q(e\,\mathrm{fm}^2)$	5.86(6)	5.3(3)[d]	4.35
			μ (nm)	−1.16(2)	−1.1778(9)[d]	−1.27
			$B(M3)$	4.4(3)		9.72
			$B(C2)$	17.1(3)		9.43
2.43	[2.43]	$5/2_1^-$	$B(C2)$	46.0(5)		32.2
			$B(M1)$	0.0090(3)		0.0068
			$B(M3)$	0.5(3)		2.22
6.38		$7/2_1^-$	$B(C2)$	33(1)	25.6(1.4)[e]	12.7
1.68	[1.68]	$1/2_1^+$	$B(C1)$	0.034(3)	0.027(2)[f]	0.0045
			$B(M2)$	0.023(8)		0.022
3.05	2.87	$5/2_1^+$	$B(C1)$	0.029(5)		0.0039
			$B(M2)$	0.16(2)		0.018
			$B(C3)$	0.9(6)		12.5
			$B(M4)$	58(3)		127.6
4.70	4.92	$3/2_1^+$	$B(C1)$			0.0006
			$B(M2)$			0.013
			$B(C3)$			3.41
6.76	6.39	$(9/2_1^+)$[g]	$B(C3)$	216(5)		17.6
			$B(M4)$	174(16)		223.8
	7.52	$5/2_2^+$	$B(C3)$			25.7
11.28	8.46	$(7/2_1^+)$[g]	$B(C3)$	57(6)		26.5
			$B(M4)$			35.9
	9.26	$3/2_3^+$	$B(C3)$			3.26
	12.01	$7/2_2^+$	$B(C3)$			4.72
			$B(M4)$			78.7

[a]Quadrupole moment, dipole moment, and reduced transition probabilities. The units of $B(CJ)$ and $B(MJ)$ are both e^2 fm^{2J}.
[b]From present PGE fits.
[c]Includes effective charges but omits scale factor applied to plotted form factors.
[d]From Ajzenberg-Selove compilation (Ref. 2).
[e]Low q (e,e') from Ref. 16.
[f]Low q (e,e') from Ref. 33.
[g]Suggested identifications.

The data for the $\frac{3}{2}^-$ and $\frac{5}{2}^-$ states are sufficient to extract the rather small transverse form factors for these states. The 180° data of Lapikas *et al.*[23] determine the elastic $M1$ form factor, whereas the present 160° data determine the elastic $M3$ form factor. Two terms are needed to describe the $M1$ at low q. The data of Clerc *et al.*[17] determine the $M1$ for the $\frac{5}{2}^-$ state. No attempt was made to fit an $M3$ form factor to the rather sparse transverse data for the $\frac{7}{2}^-$ state. Fits to these form factors are shown in Fig. 6 and the coefficients and multipole moments are listed in Tables IV and V. Shell-model calculations, shown in Fig. 7, describe the shapes of these transverse form factors quite well. For elastic scattering, the squared magnetic form factors need to be quenched by a factor of about 0.7 to reproduce the data, whereas no quenching seems to be needed for the $\frac{5}{2}^-$ state.

The absence of a detectable transverse contribution for the 6.38 MeV peak supports assignment to the ground-state rotational band. By contrast, the enhancement of the 160° data for the 6.76 MeV peak, shown in Fig. 5, strongly suggests a positive-parity assignment.

B. $C3$ excitations

The longitudinal form factors for the states at 6.76 and 11.28 MeV seem to peak further out in momentum transfer than those of the ground-state rotational band, suggesting a multipolarity of $C3$ rather than $C2$. Similarly, the transverse from factors are more important and also peak at larger momentum transfer, suggesting $M4$ dominance. Therefore, we identify the 6.76 MeV state with the lowest $\frac{9}{2}^+$ state, which is predicted to occur at an excitation energy of 6.39 MeV. Based upon the similarity between the longitudinal form factors for the 6.76

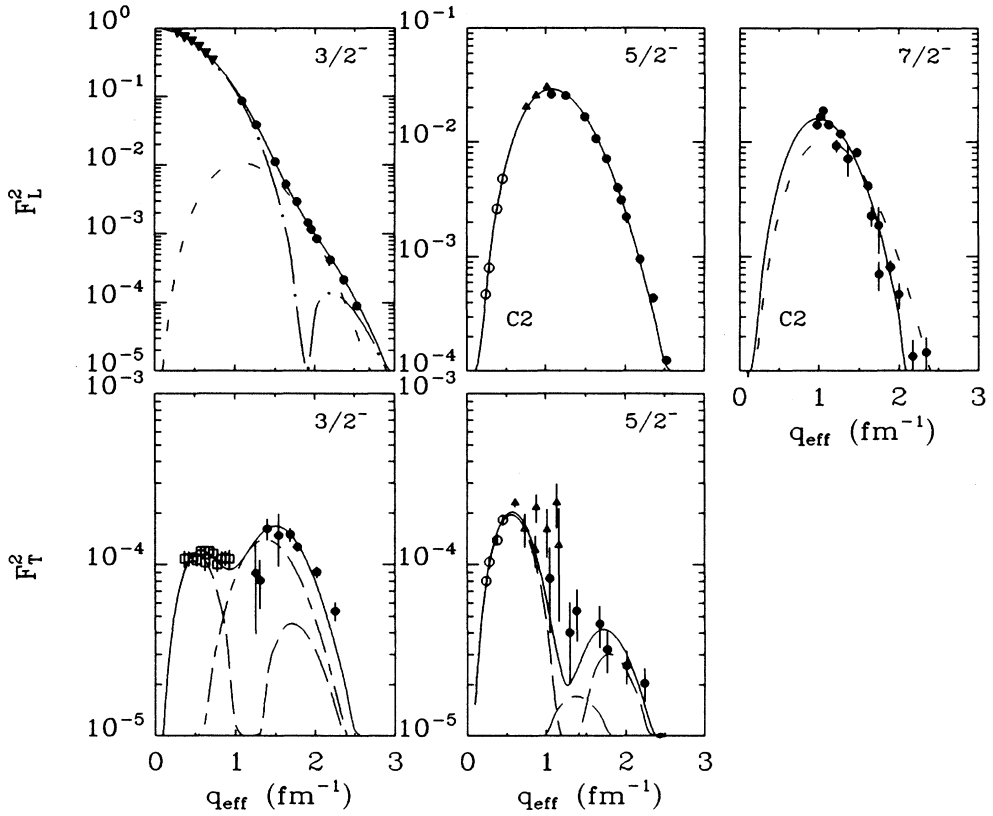

FIG. 6. PGE fits to data for members of the rotational band. Closed circles show the present data, inverted triangles the data of Jansen *et al.* (Ref. 22), open squares the data of Lapikas *et al.* (Ref. 23), solid squares the data of Clerc *et al.* (Ref. 17) and open circles the data of Ensslin *et al.* (Ref. 24). Final fits to the total form factor are shown as solid lines. The short dashed lines portray $C2$ form factors obtained by scaling the fit to the $\frac{5}{2}^-$ longitudinal form factor. The solid line for the $\frac{7}{2}^-$ state represents an independent fit to that $C2$ multipole. Other multipoles are shown as long dashes for $M1$ and as long-short dashes for $M3$.

and 11.28 MeV states, we expect the 11.28 MeV state to have a multipolarity between $\frac{5}{2}^+$ and $\frac{11}{2}^+$ ($C3$ transitions from the $\frac{3}{2}^-$ ground state). However, the energy of the lowest $\frac{11}{2}^+$ state is predicted to be 15.5 MeV and the form factor calculated for that state is much too small. Similarly, the second $\frac{9}{2}^+$ state is predicted at 14.0 MeV and also has a form factor that is too small. When compared with shell-model calculations, the absence of minima in the form factor data also tends to eliminate a $\frac{5}{2}^+$ assignment. Hence, the most likely assignment for the 11.28 MeV state is $\frac{7}{2}^+$. The lowest $\frac{7}{2}^+$ states are predicted to occur at about 8.46 and 12.01 MeV. Of these, the former gives better agreement with both the strength and the shape of the experimental form factor, but the latter cannot be excluded.

A 4% branch observed in β-delayed alpha decay from ^{9}Li suggests a negative-parity state, probably $\frac{3}{2}^-$, underlies the peak we observed at 11.28 MeV.[35] However, neither the shape nor the strength of any nearby negative-parity shell-model state is consistent with the (e,e') data. Also, the 11.81 MeV state appears to be the analog of the 12.06 MeV state populated by β^+ decay from ^{9}C (Ref. 36). The width of this state complicates interpretation of the ^{9}Li experiment. Therefore, we neglect possible $\frac{3}{2}^-$ contributions to the state observed in (e,e') at 11.28 MeV.

Shell model calculations for the lowest $\frac{9}{2}^+$ and $\frac{7}{2}^+$ states are compared with the data for the 6.76 and 11.28 MeV peaks in Fig. 8. The calculated transverse form factors are in good agreement, in both shape and magnitude, with the transverse data for both states, supporting the identification of these states as positive-parity states of relatively high spin. Note that the $E3$ and $M4$ form factors are similar in shape, but that the $E3$ dominates the $\frac{7}{2}^+$ calculation whereas $M4$ dominates the $\frac{9}{2}^+$ calculation.

On the other hand, although the calculated $C3$ form factors describe the shapes of the longitudinal data for both states, their strengths are well below the data despite use of effective charges. For the 6.76 MeV state, which is predicted to be predominantly a neutron excitation, the square of the calculated $C3$ form factor is smaller than the longitudinal data by a factor of about 10. Similarly, the $C3$ prediction for the $\frac{7}{2}^+$ state is below the

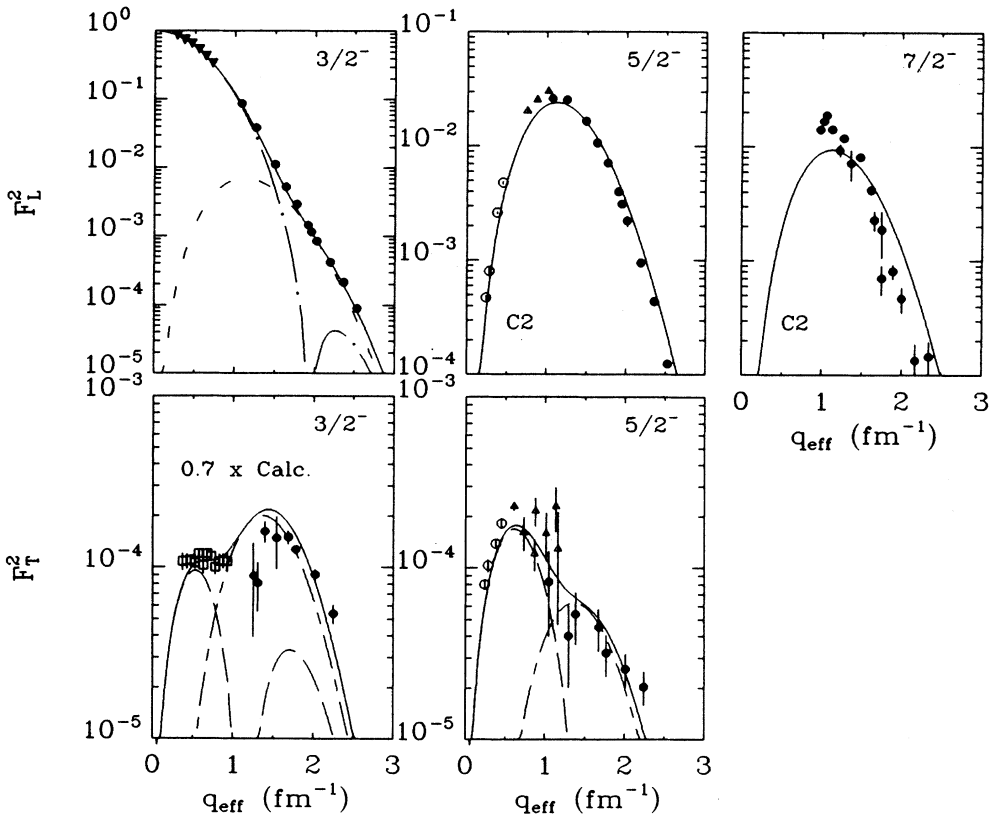

FIG. 7. Shell model calculations for the ground-state rotational band are compared with the data using the same legend as Fig. 6. The squared elastic magnetic form factor calculation has been scaled by 0.7 to give better agreement with the $M1$ data.

data by a factor of about 1.7. If these identifications are correct, the data suggest that proton transitions participate considerably more strongly than predicted, perhaps as a consequence of deformation of the single-particle potential.

However, we note that although the shapes of the form factors are well determined by this experiment, the magnitudes for both states depend strongly upon their widths. For example, if the width of the 11.28 MeV is not actually as large as the result of Dixit *et al.*,[1] the scale factor needed to bring the shell-model calculation into agreement with the data would be closer to unity. Similarly, the magnitudes for the calculated form factors depend upon wave functions at large radii which, for these broad states, may be poorly described by harmonic-oscillator orbitals. Therefore, we consider the accuracy of the calculated shapes to provide relatively strong confirmation of these assignments despite the inaccuracy of the magnitudes of the form factors.

If the identifications of the 6.76 MeV state as $\frac{9}{2}^+$ and the 11.28 MeV state as $\frac{7}{2}^+$ are correct, the longitudinal form factors should be dominated by $C3$ and the transverse by either $M4$ or $E3$ multipoles of similar shape. Fits to the data using $C3+M4$ for the 6.76 MeV state and $C3+E3$ multipoles for the 11.28 MeV state are shown in Fig. 9. A small $E3$ contribution for the 6.76 MeV state was estimated assuming irrotational flow. Although the longitudinal data do not extend to small enough momentum transfer to confirm the shapes and extract the strengths with great confidence, the successful high-q shapes tend to support our identification of $C3$ multipoles.

In the present calculation, about 90% of the $9/2_1^+$ wave function is described by weak-coupling between a valence $d_{5/2}$ neutron and the $2_1^+ T=0$ state of the ^{8}Be core. Therefore, excitation of that state is dominated by a $p \rightarrow d$ neutron transition whose $C3$ strength depends upon the neutron effective charge. Enhancement of the corresponding proton transition requires admixture of a $^8\mathrm{Li}\, 2^+ \otimes d_{5/2}$ configuration, which is difficult to accomplish in the face of a 14 MeV gap between these core states. Moreover, even if the interaction were adjusted to concentrate all $C3$ strength carried by $\frac{9}{2}^+$ states into a single state, the total strength would still be less than half the strength observed near 6.7 MeV. Therefore, three possible explanations for this concentration of $C3$ strength present themselves. First, the model space may require enlargement. Second, ground-state correlations of the type $(sd)^2p^3$ could substantially enhance the low-lying $C3$ strength. However, both of these modifications

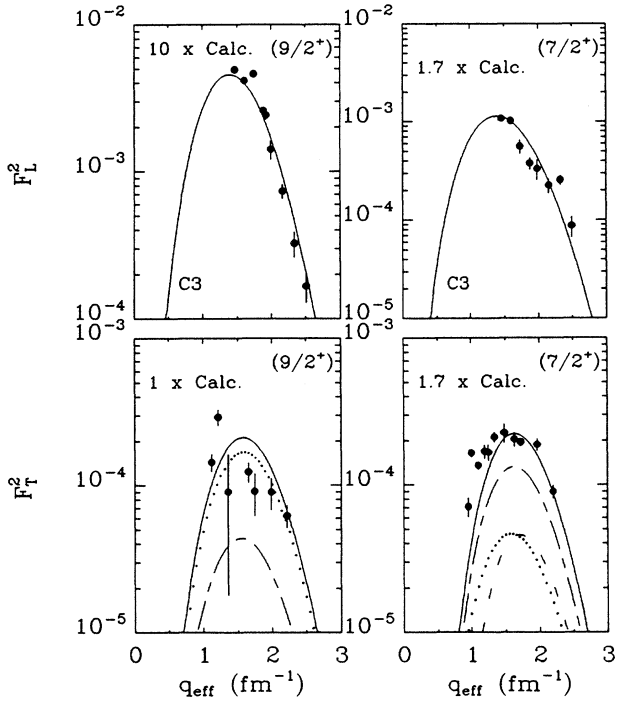

FIG. 8. Shell model calculations for the $\frac{9}{2}^+$ and $\frac{7}{2}^+$ states are compared with data for the 6.76 and 11.28 MeV peaks, respectively. Total form factors are shown as solid curves, $M2$ by short dashes, $E3$ by long-short dashes, and $M4$ by dots. Scale factors were applied to squared form factor calculations as indicated.

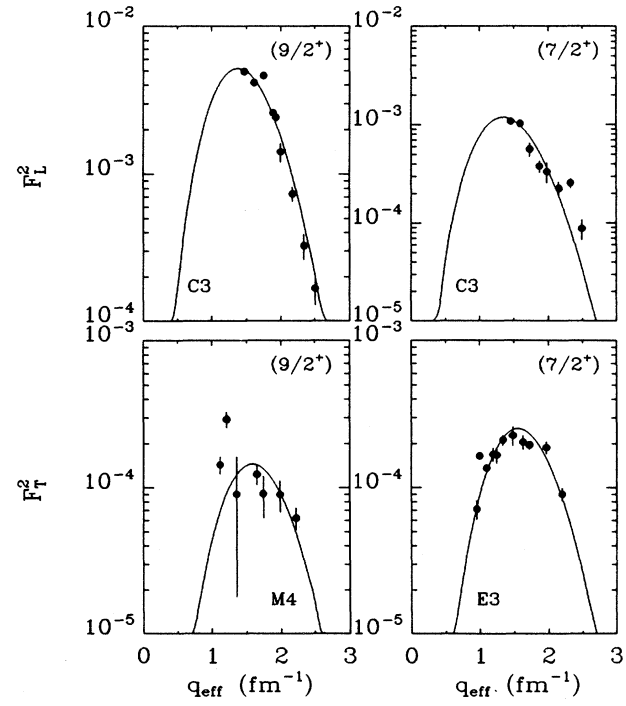

FIG. 9. PGE fits to the data for the 6.76 and 11.28 MeV states.

necessitate re-evaluation of the appropriate effective charges. Third, the observed peak may be composed of several overlapping resonances with similar form factors and a centroid near 6.76 MeV. If we assume that the $3/2_2^+$, $3/2_3^+$, $5/2_2^+$, $7/2_1^+$, and $9/2_1^+$ states all lie within this hypothetical conglomeration then, according to Table V, the summed $B(C3)$ for excitation is predicted to be about 92.3 e^2 fm^6, compared with 216(5) e^2 fm^6 observed for the 6.76 MeV peak and only 17.6 predicted for the $9/2_1^+$ state. If, in addition, we include $C1$ strength, the summed form factor 3.0×10^{-3} predicted for $q=1.4$ fm^{-1} approaches the experimental form factor 4.5×10^{-3}.

C. Low-lying positive-parity states

Shell model calculations for the $\frac{1}{2}^+$, $\frac{3}{2}^+$, and $\frac{5}{2}^+$ states are shown in Fig. 10. Phenomenological fits to the longitudinal and transverse form factors, guided by the shell-model predictions, are shown in Fig. 11.

For the $\frac{1}{2}^+$ state, the calculated $C1$ form factor peaks at a momentum transfer that is considerably too large and has a shape that is totally incorrect. However, this form factor is exquisitely sensitive to the details of the unbound radial wave function because the state lies so close to threshold.[37,38] We also observe that the spin contribution produces a rather large $E1$ form factor, but that the calculated transverse form factor also peaks at too large a momentum transfer.

For the $C1$ form factor of the $\frac{1}{2}^+$ state, we used two terms of the PGE and obtained an excellent fit to the data, which peaks at rather low momentum transfer. The first term of the $E1$ expansion was locked to the $C1$ form factor in accordance with Siegert's theorem, but the second term was allowed to vary, motivated in part by the strength of the shell model $E1$. Two terms were also fitted to the $M2$ form factor. With these three free parameters, a good description of the transverse form factor for the $\frac{1}{2}^+$ state is achieved. Good agreement with the $B(E1)$ value from (e,e') measurements at lower momentum transfer is obtained also.[33]

For the $\frac{3}{2}^+$ state, the calculated longitudinal form factor contains both $C1$ and $C3$ contributions that are similar in both strength and shape. However, these form factors are broader than the data. In fitting the data, we can not distinguish between multipoles that are so similar. Also, the 160° data are not adequate to permit analysis of the transverse form factor. Therefore, we restrict the empirical fit, somewhat arbitrarily, to $C1$ and $M2$ multipoles.

The shell model prediction for the $\frac{5}{2}^+$ longitudinal form factor is dominated at low q by $C1$ and at high q by $C3$. However, we found it difficult to extract both form factors simultaneously, especially when the data of Clerc *et al.*[17] are included. The Clerc data give a longitudinal form factor that is much larger than the shell-model calculation for low momentum transfer. When these data are included in the fit, the $C1$ form factor becomes rather strong. With only two parameters, the fitted $C1$ form

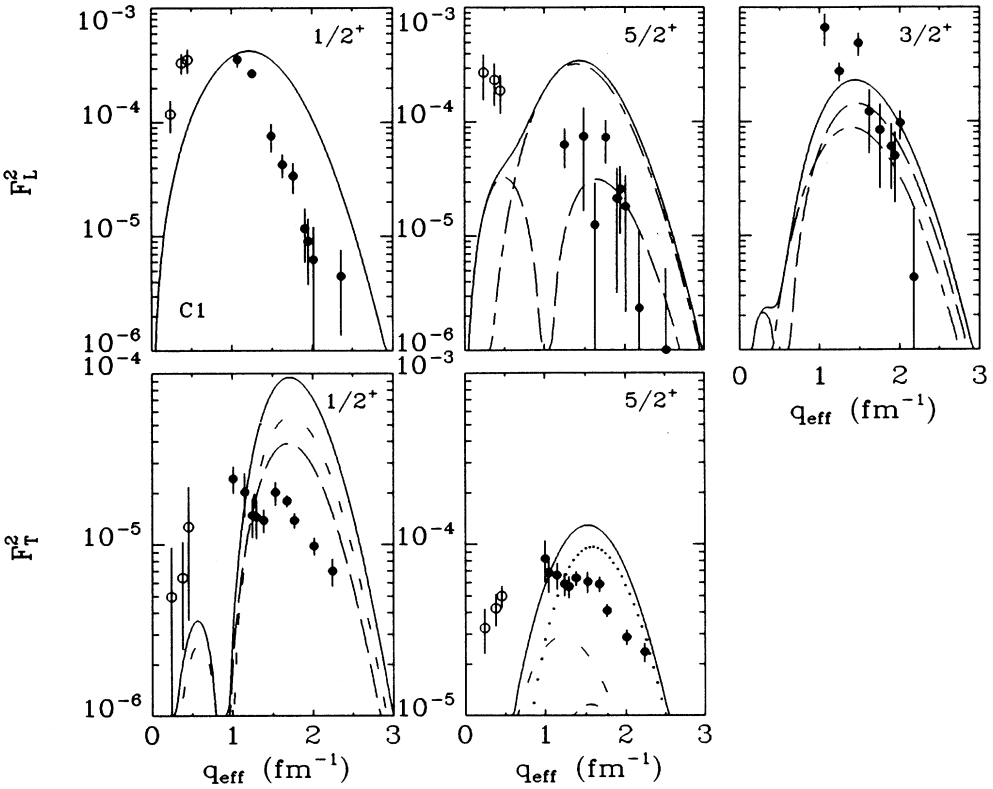

FIG. 10. Shell-model calculations for low-lying positive-parity states, using long dashes for $J=1$, short dashes for $J=2$, long-short dashes for $J=3$, dots for $J=4$, and solid curves for total form factors. The present data are shown as closed circles and those of Clerc *et al.* (Ref. 17) as open circles.

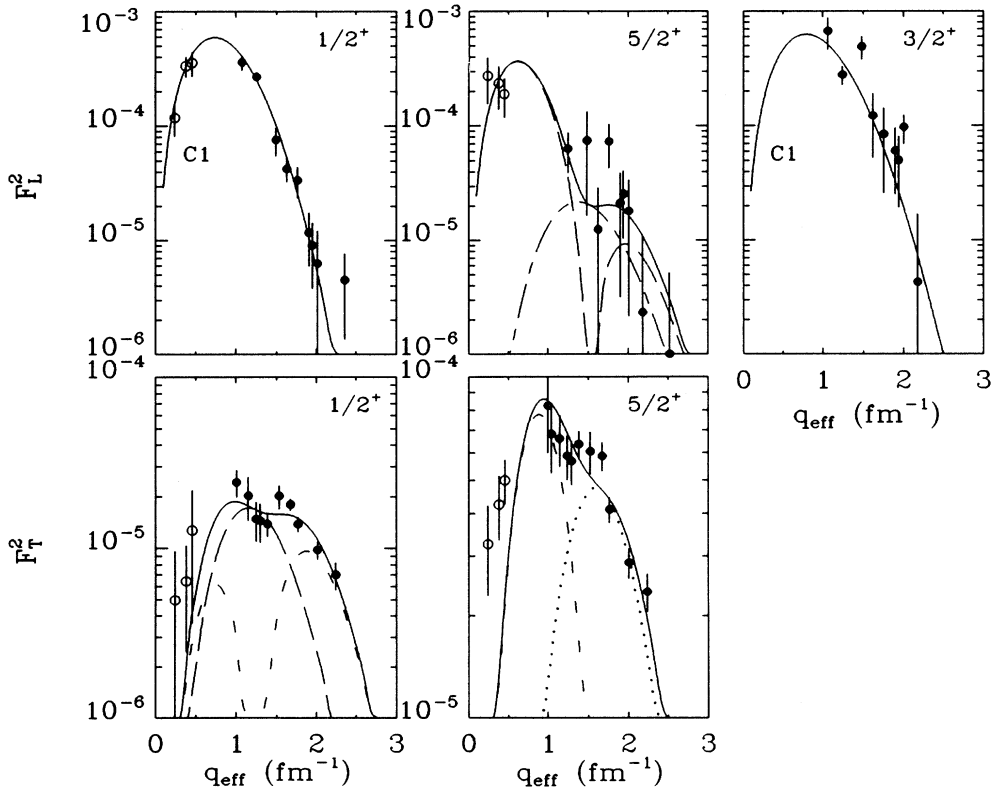

FIG. 11. PGE fits to the data for low-lying positive-parity states are shown with the same legend as Fig. 10. The $\frac{3}{2}^+$ data were fitted using only a $C1$ form factor.

factor develops a minimum near 1.5 fm^{-1} and is again strong near 2 fm^{-1}. The strength of the second maximum of the fitted $C1$ form factor interferes with extraction of the $C3$ multipole and causes the fitted $C3$ form factor to be small and uncertain. Similarly, the Clerc data for large angles require an $M2$ form factor that is considerably stronger than the shell-model prediction. Two terms for the $M2$ and one for the $M4$ form factor were used. An acceptable fit is achieved for the transverse form factor but the fit to the longitudinal form factor must be considered somewhat speculative.

D. The 13.79 MeV state

The multipolarity of the state we observe in the 160° data at an excitation energy of 13.79 MeV has not yet been established. Based upon similarities observed in the $^{11}B(p,^3He)^9Be$ and $^{11}B(p,t)^9B$ reactions and energy correspondence, it has been suggested that the ^9Be states at 11.81, 13.79, and 15.97 MeV are $J^\pi=\frac{3}{2}^-$, $T=\frac{1}{2}$ analogs of ^9B states at 12.06, 14.01, and 16.02 MeV.[39] However, the angular distributions are uncharacteristic and are consistent with any $\Delta J=2$ transition from the $\frac{3}{2}^-$ mass-11 ground state. Comparing form factors computed for several shell-model states with energies in this vicinity, we can eliminate any of the positive-parity states as variable candidates. Several negative-parity $T=\frac{1}{2}$ states with multipolarity between $\frac{3}{2}^-$ and $\frac{7}{2}^-$ produce form factors with the desired characteristics. In Fig. 12 we compare the 90° and 160° data with calculations for the third $\frac{5}{2}^-$ state, which is predicted to occur at an excitation energy of about 11.39 MeV. We find that the form factor has a predominantly $M3$ character that agrees well with the data for both 90° and 160° in both shape and magnitude. This choice also describes the (p,p') data quite well.[1] However, the $\frac{3}{2}^-$ state at 13.35, $\frac{5}{2}^-$ state at 12.87, and the $\frac{7}{2}^-$ states at 10.03 and 12.22 MeV also agree with the shape of the form factor and are within a factor of 2 of the magnitude. Therefore, we conclude that the state at 13.79 MeV is most likely a negative-parity $T=\frac{1}{2}$ state with $J^\pi=(\frac{3}{2}-\frac{7}{2})^-$ and prefer an assignment of $\frac{5}{2}^-$ based upon comparison of (e,e') and (p,p') data.

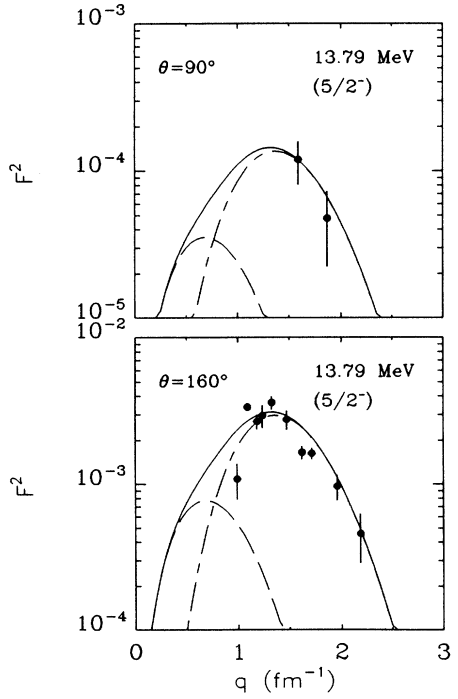

FIG. 12. Data for the 13.79 MeV state are compared with calculations for the third $\frac{5}{2}^-$ $T=\frac{1}{2}$ shell model state.

E. Narrow states above 14 MeV

Data for four states above 14 MeV that came from this experiment have previously been published by Lourie *et al.*[8] Additional data at lower momentum transfer have been reported by Bergstrom *et al.*[40] For completeness and for later use in the companion paper on (p,p'), we present form factors based upon the present shell-model calculation.

I. Negative-parity states with $T=\frac{3}{2}$

Shell model calculations for the lowest $\frac{1}{2}^-$ and $\frac{3}{2}^-$ states with $T=\frac{3}{2}$ are compared with data for their transverse form factors in Fig. 13. A scale factor of about 1.2

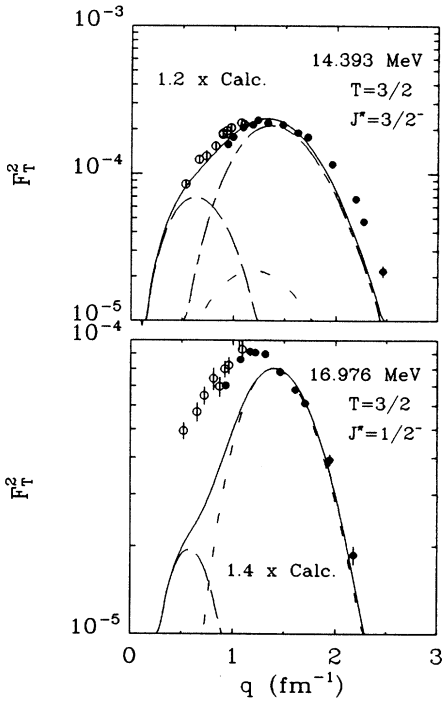

FIG. 13. Shell-model calculations for narrow $T=\frac{3}{2}$ negative-parity states are compared with the data from Lourie *et al.* (Ref. 8) (closed circles) and Bergstrom *et al.* (Ref. 40) (open circles). Total form factors are shown as solid curves, $M1$ as long dashes, $E2$ as short dashes, and $M3$ as long-short dashes. Scale factors were applied to squared form factors as indicated.

brings the $\frac{3}{2}^-$ calculation into good agreement with the data. Similarly, a scale factor of about 1.4 brings the squared $M3$ form factor into agreement with the high-q data, but the $M1$ form factor remains well below the data at low q. Although independent scaling of these $M1$ and $M3$ form factors is not sufficient to achieve agreement with the shape of the $\frac{1}{2}^-$ $T=\frac{3}{2}$ state, Woods and Barker[9] have shown that the $M1$ form factors for these states are quite sensitive to the shell-model interaction. Use of the Kumar interaction,[41] for example, results in a small decrease of the $M1$ form factor for the $\frac{3}{2}^-$ state but enhances the squared $M1$ form factor for the $\frac{1}{2}^-$ state by about a factor of 4.

It is interesting to note that the high-q data for the $\frac{3}{2}^-$ state are substantially above the $M3$ calculation, suggesting that a smaller oscillator parameter is required to fit the data. The tendency of data for magnetic form factors to be stronger at high q than calculations that use either harmonic-oscillator or Woods-Saxon wave functions based upon parameters which describe the ground-state charge density has been observed systematically throughout the p shell and the sd shell.[42,43] The highest multipole for elastic magnetic scattering is also usually described better with smaller radial scale.[44] However, unlike most shell-model calculations for magnetic excitations, this state in ^{9}Be requires a scale factor greater than unity.

2. *Positive-parity states*

The narrow states at 16.67 and 17.49 MeV were tentatively assigned positive parity and $T=\frac{1}{2}$ by Lourie *et al.*[8] Woods and Barker[9] associated the 16.67 MeV state with the $\frac{5}{2}^+$ $T=\frac{1}{2}$ state formed by coupling a $2s_{1/2}$ neutron with the lowest $2^+T=1$ excitation of the ^{8}Be core. This structure gives a relatively large $B(M2)$ and small $B(M4)$ and is narrow because of parentage based upon a relatively high-lying core excitation. Similarly, Woods and Barker associated the 17.49 MeV state with the $\frac{7}{2}^+T=\frac{1}{2}$ state formed by coupling a $d_{5/2}$ neutron to the same core configuration, resulting in a relatively large $B(M4)$ and narrow width.

States of similar structure can be found within the present shell-model calculation based upon a larger *psd* basis. The sixth $\frac{5}{2}^+$ state with $T=\frac{1}{2}$ occurs in this model at 14.9 MeV and has large $B(M2)$ and small $B(M4)$. Similarly, the fourth $\frac{7}{2}^+$ state with $T=\frac{1}{2}$ occurs at 14.8 MeV and has a large $B(M4)$. The structure of these states is described by the wave functions listed in Table VI. Both states have large coefficients for the $2^+T=1$ parent state of the core and small coefficients for low-lying core states. Significant parentages in the second $2^+T=0$ and in $1^+T=1$ and $3^+T=1$ core states are also predicted. However, because the Cohen-Kurath interaction produces excitation energies that are too small for the parent states, we can expect the calculated energies of both of these positive-parity $T=\frac{1}{2}$ states in ^{9}Be to be too low by 2–3 MeV. Hence, the identifications can be made despite the discrepancies in energy.

Form factor calculations for these model states are compared with the data in Fig. 14. The agreement between the $\frac{7}{2}^+$ calculation and the data for the 17.49 MeV state is truly remarkable. With a scale factor of about 0.7 for the squared form factor, the $\frac{5}{2}^+$ calculation is also in very good agreement with the data for the 16.67 MeV

TABLE VI. Weak-coupling amplitudes for positive-parity $T=\frac{1}{2}$ states of ^{9}Be near 17 MeV.

Configuration $J_n^\pi T\otimes sd$	J_n^π	$5/2_6^+$	$7/2_4^+$
	E_{th} (MeV)	14.85	14.84
	E_{exp} (MeV)[a]	16.671(8)	17.493(7)
		Amplitudes[b]	
$2^+T=1\otimes d_{5/2}$			0.427
$d_{3/2}$			−0.164
$s_{1/2}$		−0.606	
$2_2^+T=0\otimes d_{5/2}$			−0.308
$s_{1/2}$		−0.453	
$1^+T=0\otimes d_{5/2}$			−0.258
$3^+T=0\otimes s_{1/2}$		−0.180	−0.238
$1^+T=1\otimes d_{5/2}$		0.241	−0.327
$3^+T=1\otimes s_{1/2}$		−0.220	0.333
$d_{3/2}$		−0.120	0.142
$d_{5/2}$		0.139	

[a]Positions from Ajzenberg-Selove (Ref. 2).
[b]Only amplitudes larger than 0.1 are listed.

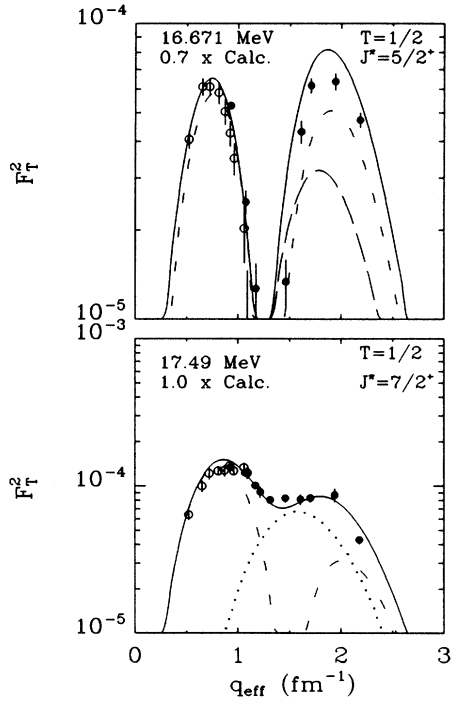

FIG. 14. Shell-model calculations for narrow $T=\frac{1}{2}$ positive-parity states near 17 MeV are compared with data from Lourie *et al.* (Ref. 8) (closed circles) and Bergstrom *et al.* (Ref. 40) (open circles). Total form factors are shown as solid curves, $E1$ as long dashes, $M2$ as short dashes, and $M4$ as dots. Scale factors were applied to squared form factors as indicated.

state, including the position of the minimum. In fact, these form factors are in better agreement with the data than those of Woods and Barker. Therefore, the present calculations support their identifications of these states.

V. SUMMARY AND CONCLUSIONS

Electron scattering data have been used to study the structure of ^{9}Be, with particular attention given to states whose large intrinsic widths have inhibited previous studies. Although line-shape uncertainties complicate this study for some states, the shapes of the form factors and the relative strengths of the longitudinal and transverse contributions are determined with useful precision.

Several new identifications have been proposed. Detailed analysis of spectra for both electron and proton scattering under similar conditions reveals that the peak listed at 6.76 MeV and identified as $\frac{7}{2}^-$ in standard compilations actually consists of two broad peaks which are excited with similar strengths. On the basis of its strong $C2$ form factor, which is consistent with both the shell model and the rotational model, we identify the state at 6.38 MeV as the $\frac{7}{2}^-$ member of the ground-state rotational band. The state at 6.76 MeV has a longitudinal form factor with characteristic $C3$ shape and a substantial transverse form factor with characteristic $M4$ shape. Therefore, we identify the 6.76 MeV state with the previously unidentified $\frac{9}{2}^+$ state predicted by the shell model. Similarly, comparisons between the data and form factors and energies predicted by the shell model suggest assignments of $\frac{7}{2}^+$ for the 11.28 MeV state and $(\frac{3}{2}^- - \frac{7}{2}^-)$ for the $T=\frac{1}{2}$ state at 13.79 MeV.

With harmonic-oscillator wave functions and standard effective charges, the shell model provides good descriptions of all of the narrow states. In particular, both the longitudinal and transverse form factors for the $\frac{3}{2}^-$ and $\frac{5}{2}^-$ states are described very well, although the elastic magnetic form factor needs to be reduced by a factor of about 0.7. The narrow negative-parity $T=\frac{3}{2}$ states are also described well. Finally, the positive-parity $T=\frac{1}{2}$ states near 17 MeV which originate in the coupling of a neutron in the sd shell to a $2^+ T=1$ excitation of the ^{8}Be core are also described quite accurately.

However, this model fails to account for the strength of the longitudinal form factors observed for the $\frac{9}{2}^+$ and $\frac{7}{2}^+$ states and fails to describe the shapes of the form factors for the low-lying positive-parity states. These difficulties for $J \leq \frac{5}{2}$ are probably due to the use of harmonic-oscillator orbitals where unbound orbitals in a highly deformed potential would be more appropriate for $C1$ excitation of broad states with positive parity. Use of more realistic radial wave functions can also be expected to improve transverse form factors for low multipoles. To increase the predicted $C3$ strength, either an enlargement of the model space or inclusion of $(sd)^2 p^3$ ground-state correlations is probably required. We might also expect $lplh$ excitations across $3\hbar\omega$ to make important isoscalar contributions to $C1$ and $C3$ transitions.

In the following paper, the scattering of 180 MeV protons is used to study these same states. Analyzing powers provide additional information on multipolarities and the comparison between (p,p') and (e,e') provides information on the relative strengths of neutron and proton transition densities. For example, from this comparison we find that the 6.76 MeV state is reached by a very nearly isoscalar transition, contrary to the shell-model prediction of neutron dominance. Therefore, the large scale factor required to reproduce the longitudinal form factor for this state indicates that the present $l\hbar\omega$ shell model does not adequately describe the isospin structure of this transition.

---

*Present address: IBM Corporation, Hopewell Junction, NY 12533.

†Present address: University of Notre Dame, Notre Dame, IN 46556.

‡Present address: University of New Hampshire, Durham, NH 03824.

§Present address: University of Washington, Seattle, WA 98195.

**Present address: LANL, Los Alamos, NM 87545.

††Present address: University of Virginia, Charlottesville, VA 22901.

[1]S. Dixit, W. Bertozzi, J. M. Finn, F. W. Hersman, C. E. Hyde-Wright, M. V. Hynes, M. A. Kovash, B. E. Norum, A. D. Bacher, G. T. Emery, C. C. Foster, W. P. Jones, D. W. Miller, B. L. Berman, J. J. Kelly, and D. J. Millener, Phys. Rev. C **43**, 1758 (1991), the following paper.

[2]F. Ajzenberg-Selove, Nucl. Phys. **A490**, 1 (1988).

[3]W. Bertozzi, T. Buti, M. Finn, C. Hyde-Wright, M. A. Kovash, R. Lourie, B. Murdock, B. Pugh, P. Ulmer, A. D. Bacher, G. T. Emery, C. C. Foster, W. P. Jones, D. W. Miller, B. Norum, J. Kelly, M. V. Hynes, B. L. Berman, W. G. Love, J. A. Carr, F. Petrovich, and F. W. Hersman, IUCF Technical and Scientific Report, 1982, p. 29.

[4]S. Dixit, M. S. thesis, Massachusetts Institute of Technology, 1986.

[5]S. Cohen and D. Kurath, Nucl. Phys. **73**, 1 (1965); T. S. H. Lee and D. Kurath, Phys. Rev. C **21**, 293 (1980).

[6]D. J. Millener and D. Kurath, Nucl. Phys. **A255**, 315 (1975).

[7]D. J. Millener, D. I. Sober, H. Crannell, J. T. O'Brien, L. W. Fagg, S. Kowalski, C. F. Williamson, and L. Lapikas, Phys. Rev. C **39**, 14 (1989).

[8]R. W. Lourie, W. Bertozzi, T. N. Buti, J. M. Finn, F. W. Hersman, C. Hyde, J. Kelly, M. A. Kovash, S. Kowalski, M. V. Hynes, B. E. Norum, and B. L. Berman, Phys. Rev. C **28**, 489 (1983).

[9]C. L. Woods and F. C. Barker, Nucl. Phys. **A427**, 73 (1984).

[10]W. Bertozzi, M. V. Hynes, C. P. Sargent, C. Creswell, P. C. Dunn, A. Hirsch, M. Leitch, B. Norum, F. N. Rad, and T. Sasanuma, Nucl. Instrum. Methods **141**, 457 (1977).

[11]W. Bertozzi, M. V. Hynes, C. P. Sargent, W. Turchinetz, and C. Williamson, Nucl. Instrum. Methods **162**, 211 (1979).

[12]H. Miska, B. Norum, M. V. Hynes, W. Bertozzi, S. Kowalski,

F. N. Rad, C. P. Sargent, T. Sasanuma, and B. L. Berman, Phys. Lett. **83B**, 165 (1979).
[13]J. J. Kelly, computer code ALLFIT (unpublished).
[14]T. N. Buti, J. Kelly, W. Bertozzi, J. M. Finn, F. W. Hersman, C. E. Hyde-Wright, M. V. Hynes, M. A. Kovash, S. Kowalski, R. W. Lourie, B. Murdock, B. E. Norum, B. Pugh, C. P. Sargent, W. Turchinetz, and B. L. Berman, Phys. Rev. C **33**, 755 (1986).
[15]J. P. Glickman, M. S. thesis, Massachusetts Institute of Technology, 1989.
[16]H. Nguyen Ngoc, M. Hors, and J. Perez y Jorba, Nucl. Phys. **42**, 62 (1963).
[17]H. G. Clerc, K. J. Wetzel, and E. Spamer, Nucl. Phys. **A120**, 441 (1968).
[18]A. G. Slight, T. E. Drake, and G. R. Bishop, Nucl. Phys. **A208**, 157 (1973).
[19]C. L. Cocke, Nucl. Phys. **A110**, 321 (1968).
[20]F. Ajzenberg-Selove, R. Middleton, and R. D. Wardaski, Nucl. Phys. **A116**, 481 (1968).
[21]D. Hasselgren, P. U. Renberg, O. Sunberg, and G. Tibbell, Nucl. Phys. **69**, 81 (1965).
[22]J. A. Jansen, R. Th. Peerdeman, and C. deVries, Nucl. Phys. **A188**, 337 (1972).
[23]L. Lapikas, G. Box, and H. deVries, Nucl. Phys. **A253**, 324 (1975).
[24]N. Ensslin, W. Bertozzi, S. Kowalski, C. P. Sargent, W. Turchinetz, C. F. Williamson, S. P. Fivozinsky, J. W. Lightbody, and S. Penner, Phys. Rev. C **9**, 1705 (1974).
[25]R. E. Rand, R. Frosch, and M. R. Yearian, Phys. Rev. **144**, 859 (1966).
[16]M. Bernheim, T. Stovall, and D. Vinciguerra, Nucl. Phys. **A97**, 488 (1967); M. Bernheim, R. Riskalla, T. Stovall, and D. Vinciguerra, Phys. Lett. **30B**, 412 (1969).
[27]T. DeForest and J. D. Walecka, Adv. Phys. **15**, 1 (1966).
[28]G. R. Hammerstein, R. H. Howell, and F. Petrovich, Nucl. Phys. **A213**, 45 (1973).
[29]A. J. F. Seigert, Phys. Rev. **52**, 787 (1937).
[30]L. J. Tassie, Austr. J. Phys. **9**, 407 (1956).
[31]D. M. Manley, B. L. Berman, W. Bertozzi, T. N. Buti, J. M. Finn, F. W. Hersman, C. E. Hyde-Wright, M. V. Hynes, J. J. Kelly, M. A. Kovash, S. Kowalski, R. W. Lourie, B. Murdock, B. E. Norum, B. Pugh, and C. P. Sargent, Phys. Rev. C **36**, 1700 (1987).
[32]J. L. Friar and W. C. Haxton, Phys. Rev. C **31**, 2027 (1985).
[33]G. Kuechler, A. Richter, and W. von Witsch, Z. Phys. A **326**, 447 (1987).
[34]A. G. Blachman and A. Lurio, Phys. Rev. **153**, 164 (1967).
[35]M. Langevin, C. Detraz, D. Guillemaud, F. Naulin, M. Epherre, R. Klapisch, S. K. T. Mark, M. de Saint Simon, C. Thibault, and M. Touchard, Nucl. Phys. **A366**, 449 (1981).
[36]D. Mikolas, B. A. Brown, W. Benenson, L. H. Harwood, E. Kashy, J. A. Nolen, B. Sherrill, J. Stevenson, J. S. Winfield, Z. Q. Xie, and R. Sherr, Phys. Rev. C **37**, 766 (1988).
[37]D. J. Millener, J. W. Olness, E. K. Warburton, and S. S. Hanna, Phys. Rev. C **28**, 497 (1983).
[38]F. C. Barker, Austr. J. Phys. **37**, 267 (1984).
[39]J. C. Hardy, J. M. Loiseaux, J. Cerny, and G. T. Garvey, Nucl. Phys. **A162**, 552 (1971).
[40]J. C. Bergstrom, I. P. Auer, M. Ahmad, F. J. Kline, J. H. Hough, H. S. Caplan, and J. L. Groh, Phys. Rev. C **7**, 2228 (1973).
[41]N. Kumar, Nucl. Phys. **A225**, 221 (1974).
[42]C. E. Hyde-Wright, W. Bertozzi, T. N. Buti, J. M. Finn, F. W. Hersman, M. V. Hynes, M. A. Kovash, J. J. Kelly, S. Kowalski, J. Lichtenstadt, R. W. Lourie, B. E. Norum, B. Pugh, C. P. Sargent, B. L. Berman, F. Petrovich, and J. A. Carr, Phys. Rev. C **35**, 880 (1987).
[43]B. L. Claussen, R. J. Peterson, and R. A. Lindgren, Phys. Rev. C **38**, 589 (1988).
[44]T. W. Donnelly and I. Sick, Rev. Mod. Phys. **56**, 461 (1984).